Simultaneous Flame, Spray, and Flow Imaging in a High Pressure Swirl Combustor

H. Ek[*], I. Chterev, N. Rock, H. Ozogul, B. Emerson, T. Lieuwen
Department of Aerospace Engineering
Georgia Institute of Technology
Atlanta, GA 30318-0150 USA

N. Jiang, S. Roy
Spectral Energies, LLC
5100 Springfield Street, Suite 301
Dayton, OH 45431

J. Gord
Air Force Research Laboratory
Wright-Patterson AFB, OH 45433

Abstract

This paper presents measurements of the simultaneous flame position and flow velocity in a high pressure, liquid fueled combustor. Liquid fuels injected in swirling flows are commonly used in gas turbines, but data collection and analysis pose a challenge in the two-phase, reacting flow field, particularly when operating at high pressure. Measurements in a liquid fueled, swirl combustor were performed using simultaneous, high speed stereo-PIV, OH-PLIF and fuel-PLIF. The OH and fuel fluorescence were separated, and regions of liquid fuel, OH and liquid fuel+OH were identified during data reduction. The measurements were taken at elevated pressures to visualize the gaseous and liquid flow field, heat release region and fuel spray distribution. This paper extends work in a prior paper by analyzing the sensitivity of the physical locations of these regimes to the processing approach.

---

[*]Corresponding author: hek6@gatech.edu

Technical Report Documentation Page

1. Report No.	2. Government Accession No.	3. Recipient's Catalog No.

4. Title and Subtitle	5. Report Date
	6. Performing Organization Code

7. Author(s)	8. Performing Organization Report No.

9. Performing Organization Name and Address	10. Work Unit No. (TRAIS)
	11. Contract or Grant No.

12. Sponsoring Agency Name and Address	13. Type of Report and Period Covered
	14. Sponsoring Agency Code

15. Supplementary Notes

16. Abstract

17. Key Words	18. Distribution Statement

19. Security Classif. (of this report)	20. Security Classif. (of this page)	21. No. of Pages	22. Price
Unclassified	Unclassified		

Form DOT F 1700.7 (8-72)   Reproduction of completed page authorized

Introduction

Increased knowledge of the highly dynamic, reacting flow fields encountered in gas turbine combustors is important to the understanding of operational limits and emissions, and how improvements in one area affect the other. High speed (kHz), spatially resolved imaging techniques, such as particle image velocimetry (PIV) and planar laser-induced fluorescence (PLIF), contribute to the understanding of the dynamic combustion environment. The morphology of unsteady, three dimensional swirling flows is better understood thanks to high speed PIV measurements [1], [2], while high speed PLIF measurements, primarily using OH, have enabled understanding of the flame location [3-6].

This paper extends work on this topic described in Chterev et al. [12], and the rest of this section and the following summarize several key points described there. There are a number of challenges associated with simultaneous OH-PLIF and fuel-PLIF measurements in high pressure, liquid-fueled, swirling combustors. OH-PLIF measurements suffer from [7-10]: (1) reduction of fluorescence yield due to increased collisional quenching (mitigated somewhat by increase in number density); (2) collisional broadening and overlap of the excitation lines; (3) fluorescence trapping due to increased optical density at high pressures; (4) laser energy absorption by liquid fuel and higher elevated gas concentrations; (5) interference from liquid fuel and unburnt hydrocarbon fluorescence resulting from fuel decomposition [11]. Our prior study [12] obtained simultaneous high speed stereoscopic PIV (sPIV), OH-PLIF and fuel-PLIF measurements in a high pressure, liquid-fueled, swirling combustor. One of the challenges addressed was the difficulty of distinguishing fuel containing regions from OH containing regions using fluorescence measurements when burning complex fuels. A specialized detection method, utilizing both temporal and spectral filtering techniques, was demonstrated. In addition, a post-processing scheme using intensity histograms was developed to provide final separation of the signals. The objective of this paper is to further consider the sensitivity of the results to the thresholds used in the separation technique.

Experimental Facility

The experimental facility used for the measurements can be seen in Figure 1. Key components include air supply and preconditioning, fuel supply, the optically accessible pressure vessel and liner, fuel injector and exhaust section.
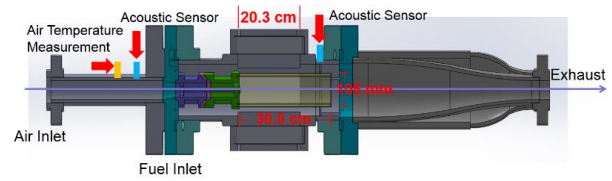

Figure 1. Schematic of combustor. Reproduced from 2017 AIAA paper no. 2017-0152 [12].

The air can be compressed up to 20 bar, and heated to temperatures ranging from 350 to 750 K, while the fuel is supplied at approximately room temperature (300-305 K). The pressurized, preheated air enters the test section through the swirler shown in Figure 2. The fuel is injected using an airblast atomizer with 6 x 0.18 mm holes spraying radially into the flow and against a filming surface. The pressure vessel has optical access through quarts windows on all four sides. The vessel houses the combustor liner, a 305 mm long quartz tube with an inner diameter of 105 mm, which contains the combustion region. Temperature and static pressure are recorded at the nozzle outlet (dump plane), which also houses a hydrogen torch igniter. The nozzle diameter is referenced in this paper as D_0. A more detailed description of the experimental facility and the instrumentation can be found in Chterev *et al* [12].
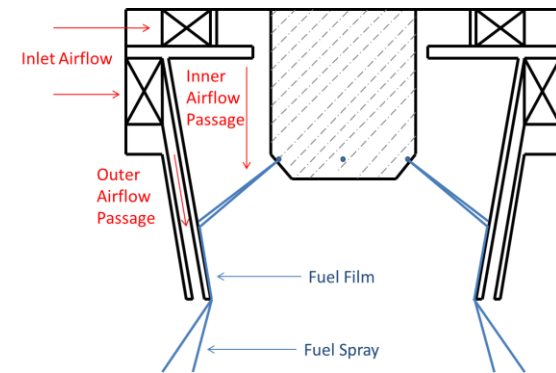

Figure 2. Schematic of swirler and airblast atomizer. Reproduced from 2017 AIAA paper no. 2017-0152 [12].

Operating Conditions

The data used for the sensitivity study are collected at a range of operating conditions and for two multicomponent fuels as summarized in Table 1. C-5 is a high aromatics fuel with low boiling point, viscosity, density and surface tension compared to Jet-A.

Table 1: Operating Conditions**.**

Case	p [bar]	T_{ph} [K]	ϕ	Nozzle velocity [m/s]	Fuel
1	2.1	450	0.38	78	Jet-A
2	3.7	451	0.38	65	C-5
3	3.4	446	0.61	78	Jet-A
5	5.2	459	0.47	75	Jet-A

Diagnostics

The PIV light source is a dual head, frequency doubled, diode pumped, solid state, Nd:YLF 527 nm laser. The pulse energy is 2 mJ with duration of approximately 200 ns and a dual pulse separation of 16 μs. A combination of cylindrical lenses is used to form a 2 mm thick and 3.70 D_0 wide laser sheet. The sheet enters through the top of the combustor and is aligned in the radial-axial (r-z) direction to within 0.5 mm of the combustor centerline. Data are collected at 5 kHz, 7500 images at a time. Imaging is performed using a pair of 12-bit Photron SA5 cameras at 10 kHz, with a resolution of 896×848 pixels. The cameras are equipped with $f = 100$ mm AT-X M100 Tokina lenses set to f/D = 11, which gives a final resolution of approximately 70 μm/pixel. A band pass filter centered at 527 nm is used to reject flame emission. The cameras are installed at an angle of approximately 45° to the laser sheet in a side-scattering configuration. This allows for equal displacement sensitivity in plane and out of plane, which is desired due to the high swirl number of the flow. Scheimpflug adaptors are used to adjust the focal plane for the angle of the cameras relative to the laser sheet. A schematic of the optical setup can be seen in Figure 3.
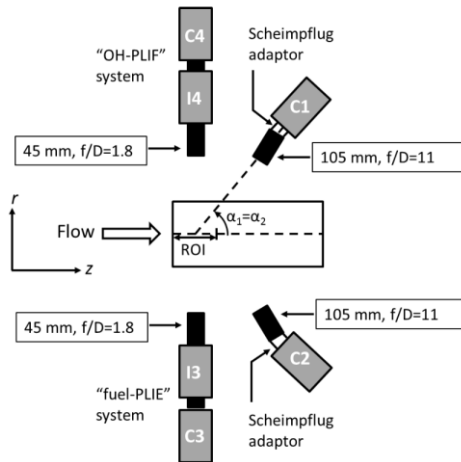

Figure 3. Optical Setup. Reproduced from 2017 AIAA paper no. 2017-0152 [12].

The seed consists of 0.5-1.0 μm TiO_2 particles. The seed is injected into the flow using a passive agitation, swirling seeder, which operates with approximately 5% of total air flow. To ensure uniform seeding density, the injection point is approximately 1.8 m upstream of the nozzle exit plane. The windows were cleaned after each run.

The cameras are registered using a dual plane dot pattern target from LaVision. Self-calibration is performed to correct for the slight misalignment between the laser sheet and the registration target facial plane. LaVision DaVis 8.1.6 is used to process the PIV images. The image pre-processing includes sliding minimum subtraction to reduce background interference, and particle size normalization to enhance the PIV code sensitivity. Multiple passes are performed, starting with an initial interrogation window size of 96×96 pixels and decreasing to a final size of 32×32 pixels. The final window size weighting function is an optimized non-uniform function. A 50 % overlap of windows is used, resulting in a vector spacing of 0.86 mm. For PIV uncertainty calculations, refer to Chterev et al. [12].

A DPSS Nd:YAG laser is operated at 5 kHz, with 5 mJ pulse energy, to pump a Sirah Credo tunable dye laser, which is frequency-doubled to yield a UV pulse energy of 300 μJ. The 566 nm output of the dye laser has a specified line width of 0.08 cm^{-1}, thus the frequency-doubled output line width is 0.11 cm^{-1}. The UV excitation is tuned to the OH $Q_1(6)$ transition of the (1,0) vibrational branch in the A-X system using a test burner, corresponding to a wavelength of 282.93 nm. The Q-branch provides strong fluorescence signals, and the $Q_1(6)$ line has a weak temperature dependence. The PLIF sheet is aligned to the sPIV sheet, having the same span but with a thinner thickness of approximately 100 μm. The laser sheets are coincident to better than ¼ of the sPIV sheet thickness, or 0.5 mm.

The imaging cameras, 12-bit Photron SA1 and NAC GX-3, are coupled to high speed image intensifiers. These are then placed normal to the laser sheet on either side of the combustor as illustrated in Figure 3. The intensifier allows for the collection of UV light while also providing gating control to minimize the interference from flame emission. An f=45mm, f/D=1.8, UV camera lens is attached to each intensifier, and spectral filters are placed in front of each lens to maximize signal separation, while rejecting the excitation wavelength.

Both spectral and temporal methods are used to separate the fuel and OH signals as illustrated in Figure 4 and Figure 5. As seen in Figure 4, the laser excitation has a narrow band (approximately 0.11 cm^{-1}). Most of the OH fluorescence is concentrated within a 15 nm band, centered around 308 nm, which corre-

sponds to the (1,0) vibrational band. The fuel fluorescence on the other hand is broad, and extends well into the visible range. Two bandpass filters are used to optimize the OH imaging, a 15 nm FWHM (full width at half minimum) filter and a 40 nm FWHM filter. The narrower filter has significant transmission into the visible spectrum, which requires the use of the broader filter. To optimize the fuel-emission, a 305 nm Schott glass long-pass filter is used. This filter rejects the excitation light only. There is no need to reject the OH-fluorescence band since the fuel emission is much brighter than the OH-PLIF.

As illustrated in Figure 5, the intensifier settings for the fuel and the OH cameras are different to promote temporal separation, which is made possible due to the difference in lifetime between fuel fluorescence and OH fluorescence. The fuel fluorescence has a much longer lifetime than the OH fluorescence. The gate controlling the intensifier on the OH camera is set to open before the laser pulse since the excitation duration (approximately 10 ns) is of the order of the OH fluorescence lifetime, and the excitation and fluorescence overlap. To maximize OH-PLIF, the intensifier gate is closed as early as possible without cutting off the OH (approximately 10 ns after the laser pulse center) in order to miss some of the fuel-PLIF tail. The intensifier gate on the fuel camera ends 30 ns after the laser pulse center in order to capture all of the long-lived fuel fluorescence. Both gates were 40 ns long. The significant portion of the intensifier gates ahead of the laser pulse has no effect on the fluorescence and was required due to the minimum gate duration limit allowed by the equipment (approximately 40 ns).
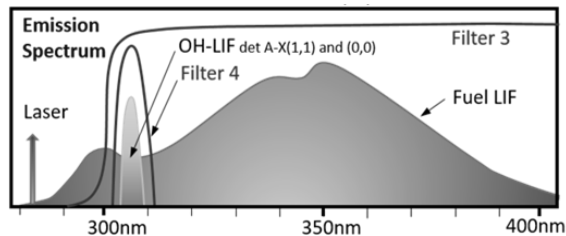

Figure 4. Separation of fuel-PLIF and OH-PLIF using spectral filtering. Reproduced from 2017 AIAA paper no. 2017-0152 [12].
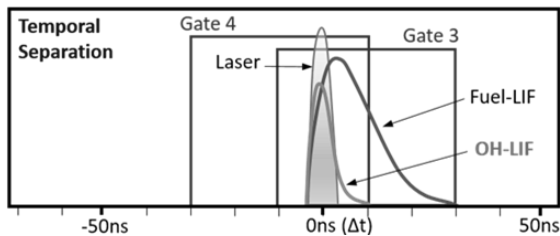

Figure 5. Separation of fuel-PLIF and OH-PLIF using temporal filtering. Reproduced from 2017 AIAA paper no. 2017-0152 [12].

The approximate resolution for the C3 camera system is 117 µm/pixel, and for the C4 system 68 µm/pixel.

Data Reduction

It is necessary to separate the fuel and OH to be able to identify the regions of spray and hot products. It would be desirable to subtract the fuel signal from the OH+fuel signal. However, the fuel emission spectrum contains both temporal and spatial variations and the intensifiers have an intrinsic non-linear response, especially at high intensities. This rules out direct subtraction as an option for signal separation. Chterev et al. [12] describes a separation method, where a mask is created based on the fuel-PLIF image, which is then applied to the OH+fuel-PLIF image. The thresholds for the fuel mask are obtained from intensity histograms. The data reduction method used by Chterev et al. is outlined below.

First, the synchronized, raw images from the fuel-PLIF camera and the OH+fuel-PLIF camera are corrected for the response of the camera/intensifier/lens system and the laser sheet profile. These corrections include: (1) dark image subtraction to compensate for the camera sensor offset at zero light; (2) flat field correction for spatial variation in the optical system intensity response; (3) time-averaged laser sheet intensity correction using acetone-PLIF; (4) image registration and LaVision self-calibration on PIV and PLIF images. Note that the laser sheet intensity correction is done *across* the beam path and not *along* the beam path. Also, the analysis is confined to the top half of the images, since the fuel and OH signals are weak in the bottom part due to laser energy absorption.

Next, an intensity histogram is computed using the top half of all of the corrected, instantaneous fuel-PLIF images for a given run. The histogram for case 1 can be seen in Figure 6. The histogram contains two distinct populations, one corresponding to weak background signal, and one corresponding to the liquid fuel emission signal. These two populations are more apparent in the bottom plot of Figure 6, which displays the derivative of the histogram (this helps identify points of inflection in the histogram, which appear as local minima/maxima in the derivative of the histogram). The histograms for the other cases look qualitatively similar to that of case 1. The multimodal distribution is believed to be linked to spray atomization physics. The weaker signal population corresponds to the distribution of fine droplets with diameters smaller than the resolution of the imaging system, allowing multiple small droplets in a given pixel. Hence, these small droplets cannot be resolved by the imaging system. The stronger signal originates from a distribution of larger droplets or ligaments, which are readily re-
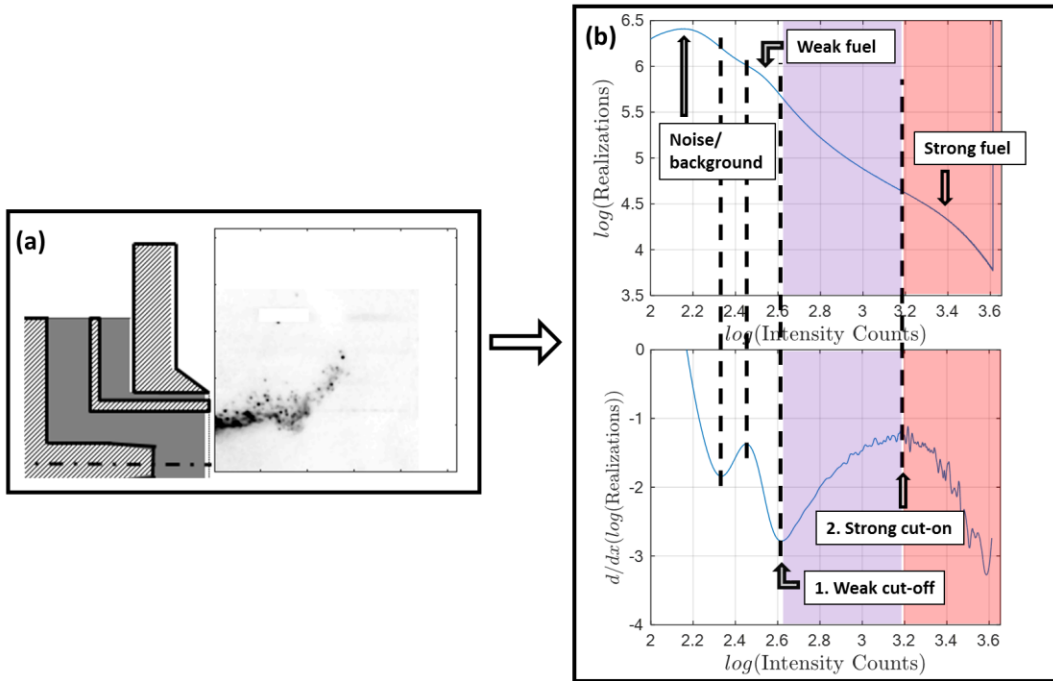
Figure 6. Instantaneous fuel-PLIF images (a) are used to calculate the intensity histogram and its derivative for case 1 (b).

solved. As shown in Figure 6, two thresholds are defined from the inflection points of the histogram. The first one is the "background cut-off" and the second one is the "signal cut-on". The detectable fuel signal corresponds to liquid fuel. The vapor fuel-PLIF is much dimmer and cannot be detected, primarily due to the difference in density. Vapor fuel-PLIF does not register on the camera within the noise/background level of 10 % of full scale for the 12-bit camera used, which is apparent from Figure 6. Similar results are obtained for the other cases. Next, using the thresholds obtained from the fuel-PLIF histogram, three regions are identified in the OH+fuel images:

a) Intensities below the "weak cut-off": there is no detectible fuel registered by the fuel-PLIF camera. Hence, any signal on the OH+fuel camera is from OH.

b) Intensities above the "weak cut-off" threshold and below the "strong fuel signal cut-on": there are smaller fuel droplets and OH, "fuel+OH" in this region.

c) Intensities above the "strong fuel signal cut-on": Any signal in this region on the OH+fuel camera is dominated by fuel. In the midst of dense regions of spray, combustion (OH production) is not expected to take place, and transport of OH to these regions is assumed negligible. It is concluded that this region contains fuel only.

The information from the fuel-PLIF and OH+fuel-PLIF can now be combined into composite, false colored images as seen in Figure 7. The red region corresponds to "fuel only", the purple region corresponds to "fuel+OH" and the blue region corresponds the presence of OH with "no detectible fuel".

Next, the blue region of "no detectible fuel" is obtained by masking the OH+fuel-PLIF images using the "weak fuel cut-off" threshold. An intensity histogram is then computed using all of the masked instantaneous OH-PLIF images. The histogram contains three distinct populations, which indicates the existence of three different regions:

a) Background emission signal

b) Spatially diffuse, low level OH signal. The low OH levels are primarily found in the inner and outer recirculation zones, which suggest that they originate from OH in recirculating product gases.

c) Elevated OH regions, which occur immediately outside the fuel jet and in plumes downstream of the flame zone. These appear to be closely associated with the super-equilibrium OH in the reaction zones.

Figure 8 shows an instantaneous masked OH-PLIF image (a), the intensity histogram and its derivative (b). The elevated OH region is defined from the inflection point. Again, the histograms are similar across all cases.
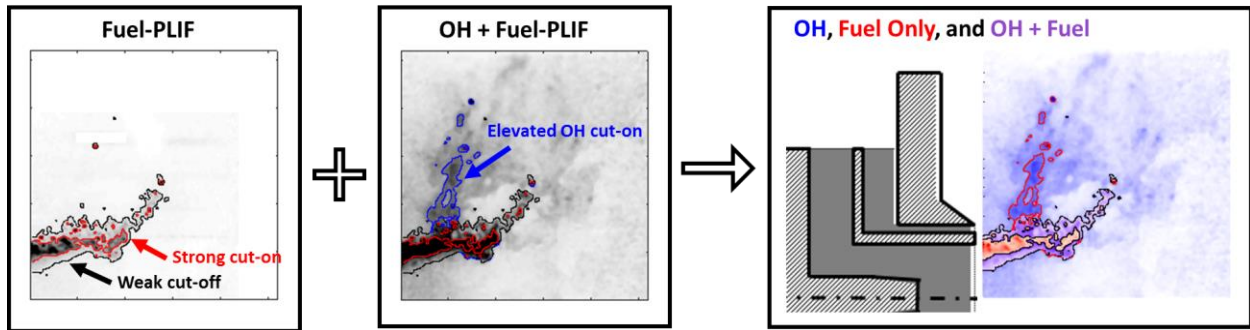
Figure 7. The thresholds from the histogram in Figure 6 are used to construct composite, false colored images. The red region contains fuel only, the purple region contains OH+fuel, and the blue region contains OH only.
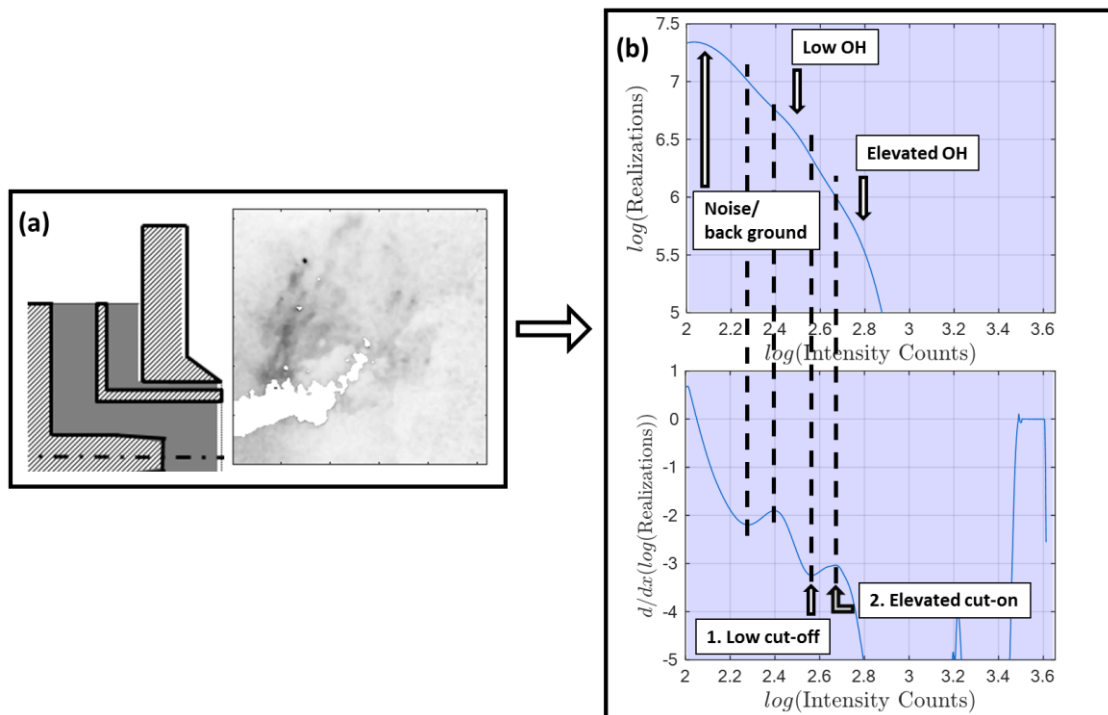

Figure 8. Instantaneous OH-PLIF images (a) are used to calculate the intensity histogram and its derivative for case 1 (b). The threshold for elevated OH is obtained from this histogram for case 1.

According to the method described above, histograms are calculated for the full datasets, using all of the instantaneous fuel images from each run listed in Table 1. Thresholds are then extracted for the strong cut-on and the weak cut-off. Next, each threshold is varied by a set of prescribed percentages, and the sensitivity in the response is observed by plotting: (1) instantaneous, false colored, composite images; (2) progress variable isocontours identifying the fuel only region and fuel+OH region.

Also, it is desirable to investigate the sensitivity of the results to the thresholds, and to estimate the uncertainties in thresholds. One potentially significant source of systematic variation in appropriate threshold

levels is intensity fluctuations. The fuel spray, which originates at the dump plane, is highly unsteady due to the nature of the turbulent, swirling combustor environment; the unsteadiness in fuel spray causes an unsteadiness in observed light intensity. To study the threshold sensitivity to spray fluctuations, the instantaneous images in each run were divided into three categories; "dim frames", "average frames" and "bright frames" according to the following criteria:

a) If the total integrated intensity is more than one standard deviation below/above the mean, the frame is categorized as "dim"/"bright".

b) If the total integrated intensity is within one standard deviation of the mean, the frame is categorized as an average intensity frame.

Figure 9 displays an example of a bright frame, an average intensity frame, and a dim frame from case 1. The same histograms as described above are calculated for these intensity-conditioned samples. Thresholds are then extracted as discussed previously, and summarized in Table 2 and Table 3. The threshold variation is calculated as the difference between the dim and the bright thresholds over their mean values. These results show that the threshold value varies by $O(10\%)$ for "fuel-only" cases, and by ~30% for the "fuel+OH" thresholds

Bright Frame:

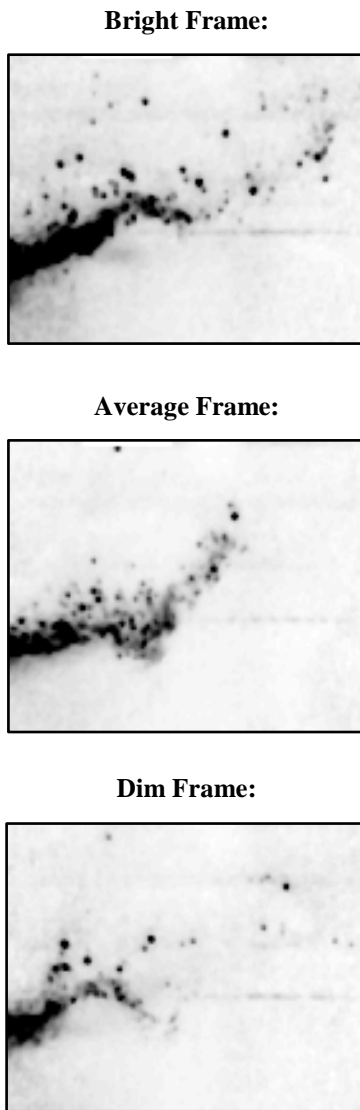**Average Frame:**

Dim Frame:

Figure 9. Example of bright, average, and dim spray frames, based on the total integrated intensity of the region of interest.

Table 2. Fuel-only thresholds extracted from the histograms calculated based on the dim and bright frame categories for each case.

	Fuel Only Thresholds		
Case	**Dim Frames**	**Bright Frames**	**Variation in Threshold (%)**
1	1510	1585	4.8
2	575	602	4.6
3	1419	2240	45
4	1550	1778	14
Avg Variation in Threshold:			**17**

Table 3. Fuel+OH thresholds extracted from the histograms calculated based on the dim and bright frame categories for each case.

	Fuel+OH Thresholds		
Case	**Dim Frames**	**Bright Frames**	**Variation in Threshold (%)**
1	447	446	0.22
2	229	275	18
3	490	832	52
4	457	679	39
Avg Variation in Threshold:			**27**

Results

The strong cut-on, which defines the fuel only region (red), and the weak cut-off, which defines the fuel+OH region (purple) are extracted from the fuel histogram calculated using all of the instantaneous fuel frames for a specific run. An upper and a lower limit are then calculated for each threshold. Based on the kinds of ranges determined for thresholds described in the prior section, these limits are obtained by varying each extracted threshold by ±10 %, ±20 % and ±30 %. The results for three instantaneous, consecutive composite images from case 1 are shown in Figure 10. The sensitivities of the thresholds are displayed as the thicknesses of the black lines bounding the fuel only regions (red) and the fuel+OH regions (purple). The threshold thicknesses are shown for ±10 % (1st row), ±20 % (2nd row), and ±30 % (3rd row) for both the fuel only threshold and the fuel+OH threshold. It is apparent that the thickness of the lines, hence the sensitivity, increases as the limits move further away from the original threshold. It can also be seen that the threshold defining the fuel only region appears less sensitive than the threshold defining the fuel+OH region. Hence, the fuel only region and the fuel+OH region

are separated by higher gradients than the fuel+OH region and OH only region. The other cases show the same trends as case 1, with Figure 11 as an example of this similarity. This figure shows a filmstrip of three instantaneous consecutive composite images for the upper and lower threshold limits corresponding to ±20% for case 3.

Case 1 can be seen to have the lowest sensitivity to spray fluctuations out of the selected cases. With a fuel only threshold variation of approximately ±2.5%, and a fuel+OH threshold variation just above ±0%, the sensitivity is below the ±10% variation shown in Figure 10, which has been verified by plotting the instantaneous composite images with the threshold isolines.

Case 3 is noted to have the highest sensitivity, with a fuel only threshold variation of approximately ±23%, and a fuel+OH threshold variation of approximately ±26%. Hence, the sensitivity due to spray intensity fluctuations in the case 3 thresholds will more closely resemble the ±20% or ±30% sensitivities shown in Figure 10. On average, however, the upper and lower limits based on the bright and dim thresholds differ by approximately 20 %, or ±10 %. Hence, this would correspond to sensitivity shown in the top row of Figure 10. On average, the sensitivity of the threshold isolines due to spray intensity fluctuations is small. The uncertainty in the location of the fuel only region and fuel+OH region is estimated to be below 1 mm on average.

Figure 12 displays the sensitivity of the 0.5 progress variables for the fuel only threshold and the fuel+OH threshold for ±10 % and ±30 %. This figure is generated based on the histogram calculated using all of the instantaneous images in Case 1. The extracted thresholds are used to generate the upper and lower limits corresponding to the ±10% and ±30% as explained previously. For each threshold, all of the instantaneous fuel images are binarized, assigning a value of unity for intensities above the specific thresh-
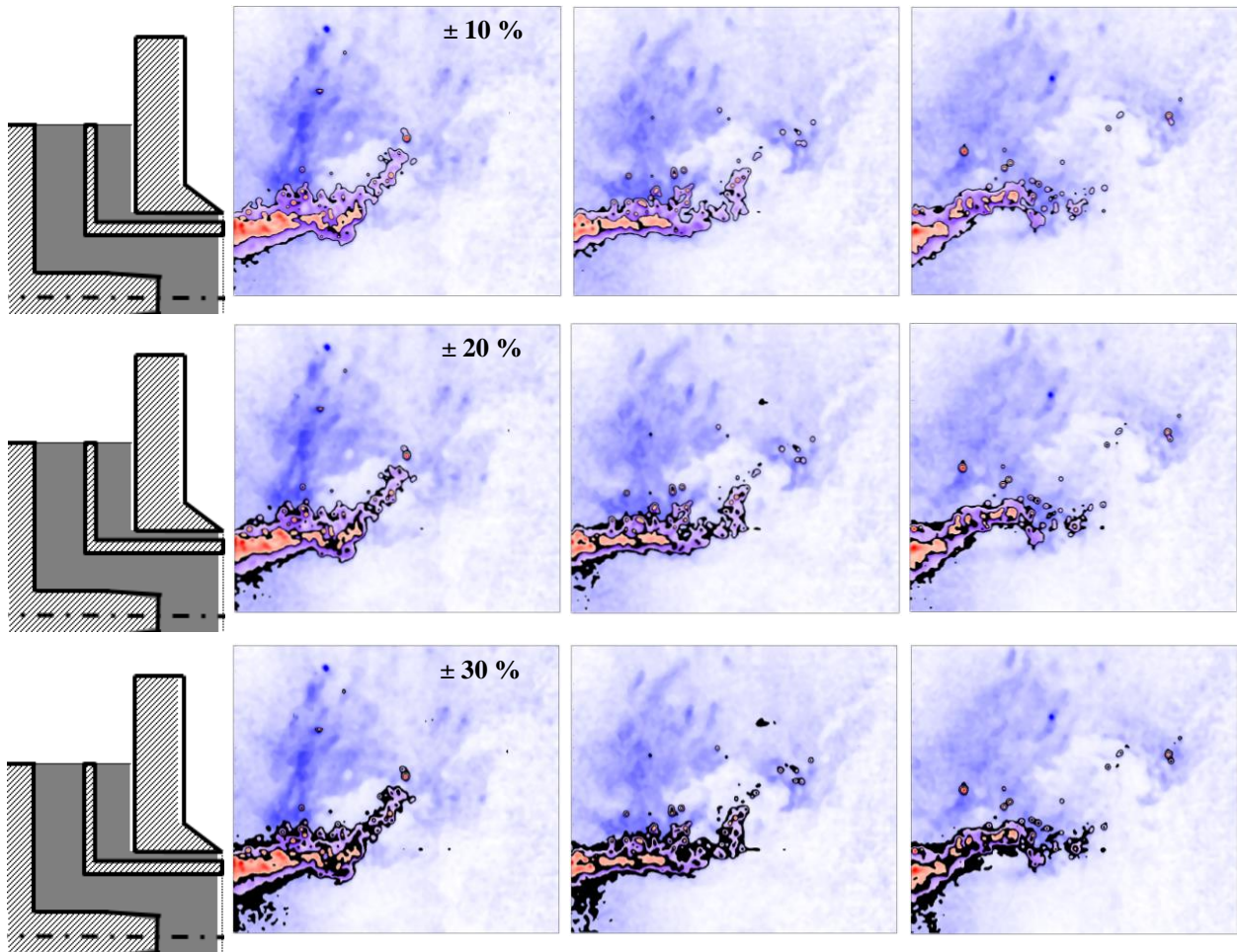

Figure 10. Filmstrips of three consecutive, instantaneous composite images from case 1. The thickness of the black threshold isolines represents the difference between upper and lower threshold limits. The thresholds are calculated based on the full dataset.
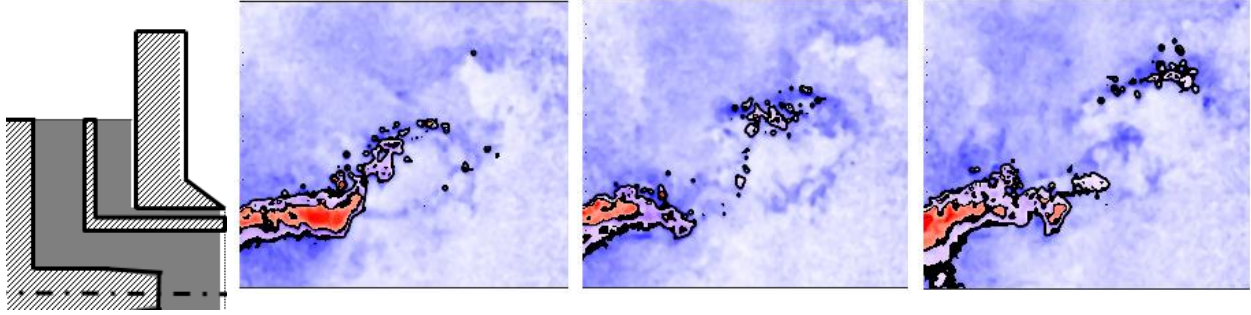
Figure 11. Filmstrips of three consecutive, instantaneous composite images from case 3. The thickness of the black threshold isolines represents the difference between upper and lower threshold limits for ±20%. The thresholds are calculated based on the full dataset.

old and a value of zero for intensities below the specific threshold. These binarized images are then summed up and averaged over the number of total frames, which generates a progress variable field for each threshold, designated $\bar{P}$. The $\bar{P}_1 = 0.5$ line corresponds to 50% probability of finding detectible fuel, while the $\bar{P}_2 = 0.5$ line corresponds to 50% probability of finding fuel only. Outside the $\bar{P}_1 = 0.5$ line, the region contains mainly OH, hence, this line can be thought of as the OH boundary. Inside the $\bar{P}_2 = 0.5$ line, the region contains mainly fuel, hence, it can be thought of as the fuel spray boundary.

The progress variables $\bar{P}_1 = 0.5$ and $\bar{P}_2 = 0.5$ are used to study the average threshold sensitivity in OH boundary location and fuel spray location respectively. Looking at the upper and lower limits corresponding to ±10 % in Figure 12, it is apparent that the sensitivity in fuel spray penetration in the axial direction (red lines) is slightly below 2.5 mm, while the sensitivity in axial location of the OH boundary (purple lines), is
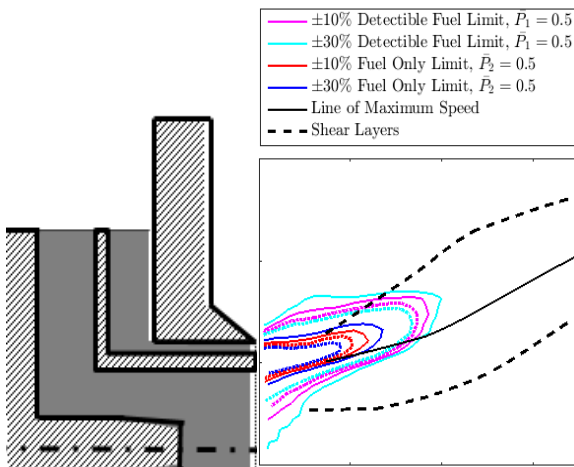

Figure 12. $\bar{P}_2 = 0.5$ for the upper and lower limits of the fuel only threshold, and $\bar{P}_1 = 0.5$ for the upper and lower limits for the fuel+OH threshold, case 1. The thresholds are calculated from the full dataset.

slightly below 1.5 mm. Looking at the upper and lower limits corresponding to ±30 %, the sensitivity in the axial fuel spray penetration (blue lines) has increased to ~4.5 mm, while the sensitivity in axial location of the OH boundary (light blue lines), has increased to ~3.5 mm. The sensitivity in the thickness of the spray region is negligible for ±10%. The sensitivity increase slightly for ±30%, but is still small in comparison to the penetration sensitivity. The width of the OH boundary shows greater sensitivity than that for the fuel only region. This is especially true for threshold limits of ±30%, where the sensitivity in width is approximately the same as the axial sensitivity.

Figure 13 displays the sensitivity in the detectible fuel limits (top) and the fuel only limits (bottom) corresponding to ±10% for different values of the progress variables $\bar{P}_1$ and $\bar{P}_2$. The sensitivity in the detectible fuel threshold appears to be independent of the $\bar{P}_1$ values with one exception; $\bar{P}_1 = 0.2$ for the +10% limit close to the nozzle centerline. For the fuel only threshold, it appears that the sensitivity in axial fuel penetration decrease as $\bar{P}_2$ decrease. However, this is a subtle difference.

Concluding Remarks

Interpretation of fluorescence measurements in a liquid fueled system is complicated by the fact that there are multiple sources of emission. Prior work from our group has proposed an approach for separating the OH- and fuel- containing regions. Nonetheless, it must be admitted that the thresholds used to delineate these different regions, while rigorously defined, are still subject to some debate. This paper has clearly shown that the key conclusions and spray and flame structures derived from these thresholding approaches are robust to reasonable variations in threshold values. This result is significant, as it shows that conclusions about relative location of fuel, flame, and velocity features can be gained from the types of measurements described here.
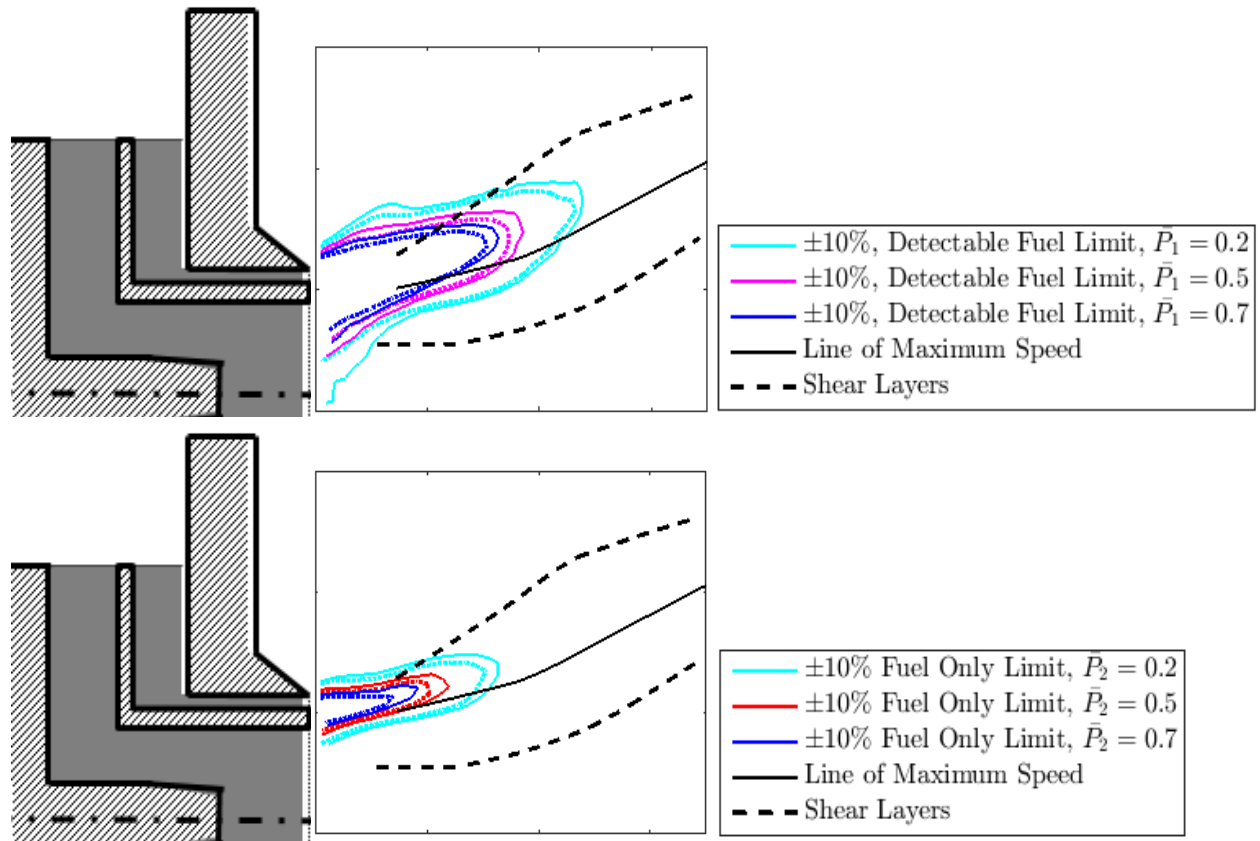
Figure 13. The plots shows the 0.2, 0.5 and 0.7 progress variable isocontours for ±10% of the detectible fuel threshold (top) and the fuel only threshold (bottom), case 1. The thresholds are calculated from the full dataset.

References

1. A. Upatnieks, J. F. Driscoll, and S. L. Ceccio, 'Cinema Particle Imaging Velocimetry Time History of the Propagation Velocity of the Base of a Lifted Turbulent Jet Flame', in Proc. Combust. Inst. (2002), pp. 1897-903.

2. A. M. Steinberg, J. F. Driscoll, and S. L. Ceccio, 'Measurements of Turbulent Premixed Flame Dynamics Using Cinema Stereoscopic PIV', Exp. Fluids, 44 (2008), pp. 985-99.

3. M. Tanahashi, S. Murakami, G. M. Choi, Y. Fukuchi, and T. Miyauchi, 'Simultaneous CH–OH PLIF and Stereoscopic PIV Measurements of Turbulent Premixed Flames', in Proc. Combust. Inst. (2005), pp. 1665-72.

4. C. Arndt, A. Steinberg, I. Boxx, W. Meier, M. Aigner, and C. Carter, 'Flow-Field and Flame Dynamics of a Gas Turbine Model Combustor During Transition Between Thermo-Acoustically Stable and Unstable States', in Turbo Expo (2010).

5. A. Steinberg, I. Boxx, M. Stöhr, W. Meier, and C. Carter, 'Effects of Flow Structure Dynamics on Thermoacoustic Instabilities in Swirl-Stabilized Combustion', AIAA, 50 (2012).

6. M. Shimura, T. Ueda, G. M. Choi, M. Tanahashi, and T. Miyauchi, 'Simultaneous Dual-Plane CH PLIF, Single-Plane OH PLIF and Dual-Plane Stereoscopic PIV Measurements in

Methane-Air Turbulent Premixed Flames', in Proc. Combust. Inst. (2011), pp. 775-82.

7. J. M. Seitzman and R. K. Hanson, 'Comparison of Excitation Techniques for Quantitative Fluorescence Imaging of Reacting Flows', AIAA, 31 (1993), pp. 513-19.

8. Brett E. Battles and Ronald K. Hanson, 'Laser-Induced Fluorescence Measurements of NO and OH Mole Fraction in Fuel-Lean, High-Pressure (1–10 atm) Methane Flames: Fluorescence Modeling and Experimental Validation', Quantitative Spectroscopy and Radiative Transfer, 54 (1995), pp. 521-37.

9. Hideaki Kobayashi, Yasuo Oyachi, and Kaoru Maruta, 'LIF Measurements of Turbulent Premixed Flames in a High Pressure Environment', in Joint Thermal Engineering Conference (1999).

10. G. Singla, P. Scouflaire, C. Rolon, and S. Candel, 'Planar Laser-Induced Fluorescence of OH in high-Pressure Cryogenic LOx/GH 2 Jet Flames', Combust. Flame, 144 (2006), pp. 151-69.

11. A. Lantz, R. Collin, J. Sjöholm, Z.S. Li, P. Petersson, and M. Aldén, 'High-Speed Fuel/Hydroxyl Radical Imaging in a Gas Turbine Pilot Burner', AIAA, 50 (2012), pp. 971-75.

12. I. Chterev, N. Rock, H. Ek, B. Emerson, J. Seitzman, N. Jiang, S. Roy, T. Lee, J. Gord, T. Lieuwen, 'Simultaneous High Speed (5 kHz) Fuel-PLIF, OH-PLIF and Stereo PIV Imaging of Pressurized Swirl-Stabilized Flames using Liquid Fuels', 55th AIAA Aerospace Science Meeting, 2017 AIAA paper no. 2017-0152